1   **Revision 1:**

2   **Magnetite exsolution in ilmenite from the Fe-Ti oxide gabbro in the Xinjie**

3   **intrusion, SW China**

4

5   **Wei Tan[1,2], Hongping He[1,2], Christina Yan Wang[1,2*], Huan Dong[1],**

6   **Xiaoliang Liang[1,2], Jianxi Zhu[1,2]**

7   [1]Key Laboratory of Mineralogy and Metallogeny, Guangzhou Institute of Geochemistry,

8   Chinese Academy of Sciences, Guangzhou 510640, China

9   [2]Guangdong Provincial Key Laboratory of Mineral Physics and Materials, Guangzhou

10   510640, China

11

12   **ABSTRACT**

13   This study investigates magnetite exsolution in ilmenite from Fe-Ti oxide gabbro

14   in the Xinjie intrusion, SW China. Exsolved magnetite lamellae in ilmenite contain

15   nearly pure Fe_3O_4 with ~1 wt% TiO_2. EBSD-based analyses indicate that the

16   magnetite lamellae have close-packed oxygen planes and directions parallel to those

17   in the host ilmenite with $\{111\}_{Mag}$ // $(0001)_{Ilm}$ and $<110>_{Mag}$ // $<10\text{-}10>_{Ilm}$. The Fe^{2+}

18   in the magnetite lamellae is probably derived from adjacent titanomagnetite by

19   sub-solidus inter-oxide cation repartitioning of $Fe^{2+} + Ti^{4+} = 2Fe^{3+}$ during cooling. It is

20   thus suggested that only Fe^{3+} cations in the magnetite lamellae should be included

21   into the composition of the Ilm-Hem$_{ss}$ precursor for the Fe-Ti oxide oxy-thermometer.

22 The existence of magnetite exsolution in ilmenite also provides an alternative

23 explanation for unusually strong natural remnant magnetization in natural ilmenite.

24 **Keywords:** Magnetite exsolution, ilmenite, Electron backscatter diffraction

25 (EBSD), crystallographic relationship, sub-solidus cation repartitioning

26

27 **INTRODUCTION**

28 Ilmenite-hematite solid solution (Ilm-Hem$_{ss}$) forms in a wide range of temperature

29 and oxygen fugacity due to the hetero-valent isomorphous substitution of $2Fe^{3+} \rightarrow$

30 $Ti^{4+} + Fe^{2+}$ (Buddington and Lindsley 1964; Evans et al. 2006; Lindsley 1991; Lattard

31 et al. 2005; Sauerzapf et al. 2008). Ilm-Hem$_{ss}$ plays an important role in the

32 acquisition of natural remanent magnetization (NRM) in different types of rocks

33 containing Ilm-Hem$_{ss}$ (Brownlee et al. 2010; Feinberg et al. 2005; Ferré et al. 2013;

34 Harrison et al. 2000; McEnroe et al. 2001, 2002). The composition of Ilm-Hem$_{ss}$ and

35 coexisting titanomagnetite can also be used as a thermometer/oxy-barometer to

36 estimate the formation temperature and oxygen fugacity of host rocks (Andersen and

37 Lindsley 1988; Buddington and Lindsley 1964). As temperature decreases, Ilm-Hem$_{ss}$

38 commonly separates into hematite-rich and ilmenite-rich end-member phases due to

39 a miscibility gap at 600–700 °C (Harrison et al. 2000), resulting in formation of an

40 intergrowth composed of oriented hematite lamellae in host ilmenite ($Fe^{2+}TiO_3$), a

41 common feature in mafic-ultramafic intrusions (Bolle et al. 2014; Harrison et al. 2000;

42 Lindsley 1991; Morisset et al. 2010).

2

43   Natural ilmenite also contains magnetite exsolution (Buddington and Lindsley

44   1964; Lattard 1995; Mücke 2003; Wang et al. 2008). Magnetite ($Fe^{2+}Fe^{3+}_2O_4$) contains

45   both Fe^{2+} and Fe^{3+}, whereas hematite ($Fe^{3+}_2O_3$) only contains Fe^{3+}. Exsolved

46   magnetite lamellae in ilmenite thus plays a key role in the Fe^{2+}/Fe^{3+} ratio of the

47   composition of Ilm-Hem$_{ss}$ precursor, which can be reconstructed by integrating and

48   averaging the chemistry of the exsolved phases and host ilmenite, and is crucial to

49   the Fe-Ti oxide oxy-thermometer. Magnetite is considered to control magnetic

50   anomalies of rocks (Frost 1991), magnetite exsolution in ilmenite may thus explain

51   the unusually strong NRM of ilmenite in some metamorphic and igneous rocks

52   (McEnroe et al. 2002; Robinson et al. 2002, 2004).

53   A number of mineralogical and geophysical studies have dealt with Fe-Ti oxide

54   exsolution in silicate minerals such as pyroxene, plagioclase and olivine

55   (Dobrzhinetskaya et al. 1996; Feinberg et al. 2004; Fleet et al. 1980; Hwang et al.

56   2008; Prior et al. 1999; Wenk et al. 2011). However, magnetite exsolution in ilmenite

57   is more or less neglected compared with hematite exsolution in ilmenite and

58   magnetite exsolution in silicates. This is probably because the magnetite lamellae in

59   ilmenite are not easily distinguished from hematite lamellae in terms of morphology,

60   optical color and BSE images (Bolle et al. 2014; Haggerty 1991; Morisset et al. 2013;

61   Wang et al. 2008). Nevertheless, the origin of magnetite exsolution in ilmenite

62   remains controversial, and has been ascribed to three mechanisms: direct exsolution

63   from Fe_3O_4-$FeTiO_3$ precursors (Mücke 2003), sub-solidus reduction of Fe_2O_3 in

3

64   Ilm-Hem$_{ss}$ (Brownlee et al. 2010; Buddington and Lindsley 1964; Haggerty 1991), or

65   sub-solidus cation repartitioning between coexisting Fe-Ti oxides (Lattard 1995).

66   In this study, magnetite exsolution is observed and confirmed in ilmenite from

67   the Fe-Ti oxide gabbro in the Xinjie intrusion (SW China) using Raman spectroscopy

68   and electron microprobe analysis (EMPA). The crystallographic relationship

69   between the crystal lattices of the magnetite lamellae and host ilmenite was

70   revealed by electron backscatter diffraction analysis (EBSD). This study has

71   important implications for understanding the mechanism of magnetite exsolution in

72   ilmenite and the major controls on the complex sub-solidus Fe-Ti oxide

73   re-equilibration.

74

75   **GEOLOGICAL SETTING AND SAMPLE DESCRIPTION**

76   The Panxi region in the central part of the ~ 260 Ma Emeishan large igneous

77   province is the most important Fe-Ti-V metallogenic district in China. Fe-Ti

78   oxide-bearing, mafic-ultramafic layered intrusions, including Panzhihua, Hongge,

79   Baima, Xinjie and Taihe, are exposed along several major N-S trending faults in the

80   Panxi region (Fig. 1a) (Wang et al. 2008; Zhou et al. 2002, 2005). The Xinjie intrusion

81   contains an ultramafic portion with minor amounts of Fe-Ti oxides in the lower part

82   and a gabbro portion with large amounts of Fe-Ti oxides in the upper part of the

83   intrusion (Zhong et al. 2004). The Xinjie intrusion is well differentiated with weakly

84   developed igneous layering, and comprises, from the base upwards, a marginal zone

4

85   and three Units (I, II and III) with differing mineral assemblages (Fig. 1b) (Dong et al.

86   2013). Units I and II are mainly composed of clinopyroxenite and wehrlite, whereas

87   Unit III is mainly composed of Fe-Ti oxide gabbro and leucogabbro (Fig. 2a) (Dong et

88   al. 2013). The samples in this study were collected from the Fe-Ti oxide gabbro in

89   Unit III. The samples contain 15-45 vol% titanomagnetite and 15-20 vol% coexisting

90   ilmenite.

91

92   **ANALYTICAL METHODS**

93   Back-scattered electron (BSE) images and compositions of minerals were

94   obtained from polished thin sections using a JEOL-JXA8230 electron microprobe

95   analyzer (EMPA) at the Guangzhou Institute of Geochemistry (GIG), Chinese Academy

96   of Sciences (CAS). Analyses were performed using an accelerating voltage of 15 kV

97   and a current of 20 nA, with a beam of 1 μm. The standards used were almandine

98   garnet for Si and Mg, pyrope garnet for Al, magnetite for Fe, rhodonite for Mn,

99   metallic Ni for Ni, metallic V for V, synthetic Cr_2O_3 for Cr and rutile for Ti. X-ray matrix

100   corrections were based on a routine ZAF method.

101   Raman spectra were obtained on a RM2000 laser Raman spectrometer at GIGCAS

102   using a 514.5 nm Ar ion laser. The laser spot is ~2 μm in diameter. The spectra were

103   collected in a range of 100 to 1600 cm^{-1}. The reproducibility of peaks was checked

104   using a silicon wafer standard before examination. Position variations for Raman

105   peaks are within 2 cm^{-1}. The laser power and acquisition time were carefully

5

106   controlled to avoid laser-induced thermal effects and oxidation (Shebanova and Lazor

107   2003a).

108   EBSD measurements were carried out in the FESEM Laboratory, China University

109   of Geosciences (Beijing) using a Zeiss SUPRA 55 FESEM with an Oxford NordlysNano

110   EBSD acquisition camera. The measurements were collected using an accelerating

111   voltage of 20 kV, 200 nA beam current and a working distance of 7-10 mm. The

112   sample surface was tilted 70° relative to horizontal to enlarge beam-specimen

113   activation surface so that EBSD signal can be enhanced. Diffraction patterns were

114   manually collected, and automatically indexed in real-time using the AZtec software

115   from the HKL Technology, Oxford Instruments. Five to eight Kikuchi bands were

116   included for the fitting algorithm. Only measurements with mean angular deviation

117   (MAD) values below 1.2° were accepted for analyses, and the indexing rate is about

118   70%. Orientation data of exsolved magnetite lamellae and host ilmenite are grouped

119   for each individual grain (electronic supplementary materials Fig. S2).

120

121   **RESULTS**

122   **Mineralogical characteristics**

123   In the Xinjie intrusion, primary ilmenite with magnetite lamellae is adjacent to

124   primary titanomagnetite with trellis-type ilmenite lamellae, forming so-called reverse

125   host-guest intergrowth of magnetite and ilmenite (Mücke 2003). The magnetite

126   lamellae in ilmenite are subparallel, and occupy 10 to 15 vol% of the ilmenite grain

6

127   (Fig. 2b). The magnetite lamellae appear as lentiform particles, thin plates or ultrafine

128   blades, with lengths varying from several to tens of micrometers. The aspect ratios of

129   the lamellae vary from 5:1 to 50:1, and short lamellae tend to have low aspect ratios

130   (Figs. 2c-e). The variation in morphology is ascribed to the balance between surface

131   energy and strain energy in the formation of the magnetite lamellae. The surface

132   energy is minimized by expelling the lamellae to form elliptical/lentiform

133   morphologies, whereas the strain energy is minimized by forcing the lamellae to

134   change into plate-/blade-like morphologies (Price 1980).

135   In the Xinjie intrusion, magnetite lamellae occur in the central part of the host

136   ilmenite with a lamellae-free halo, which is outlined by the red dashed line in Figs. 2d

137   and 2e. As outlined by the green dashed line in Fig. 2e, thick magnetite lamellae (tens

138   of micrometers wide) are also surrounded by a lamellae-free zone, indicating that the

139   thick lamellae were coarsened by absorbing surrounding thin lamellae (Joesten

140   1991).

141   **Phase identification**

142   Raman spectra were collected for the lamellae with different morphology in host

143   ilmenite. The lamellae have widths ranging from > 10 μm to ~1 μm (Figs. 2c-e). As

144   magnetite and hematite have remarkably distinct Raman features (Wang et al.

145   2004), the broad lamellae in host ilmenite are easily identified. Raman spectra of

146   lamellae with the widths of >2 μm displayed the characteristic peaks of magnetite

147   (Shebanova and Lazor 2003b), including two strong peaks at ~670 and ~545 cm^{-1},

148 and a weaker at ~308 cm^{-1}, the position variations for Raman peaks of these lamellae

149 are within 2 cm^{-1} (Fig 3a). Characteristic vibrations of hematite at ~292, ~410 and

150 ~1320 cm^{-1} (Wang et al. 2004; Tan et al. 2015a) were not observed, suggesting that

151 the >2 μm-wide lamellae in host ilmenite are mainly composed of magnetite rather

152 than hematite.

153 Raman spectra of ultrafine lamellae with widths of ~1 μm exhibited slightly

154 different features from those with widths of >2 μm. They have a broadened band at

155 ~674 cm^{-1} and two extra bands at ~227 and ~333 cm^{-1} (Fig 3a). However, our

156 peak-fit analysis (Fig 3b) show that the broadened peak at ~674 cm^{-1} may be an

157 overlap of the two peaks at ~669 and ~683 cm^{-1}, corresponding to the characteristic

158 peaks of magnetite and the host ilmenite, respectively (Wang et al. 2004). The two

159 extra peaks at ~227 and ~333 cm^{-1} are fit well with those of the host ilmenite (Fig

160 3b). Hence, the results of Raman spectra indicate that all the lamellae in host ilmenite

161 are magnetite despite their different size and morphology.

162 **Chemical composition**

163 As EMPA is unable to distinguish between Fe^{3+} and Fe^{2+}, both Fe_2O_3 (Fe^{3+}) and

164 FeO (Fe^{2+}) in iron oxides are expressed as ΣFeO (Table 1). Redistribution of Fe_2O_3

165 and FeO in ΣFeO is based on the charge balance and stoichiometry of ilmenite and

166 magnetite, respectively. The EMPA results indicate that the host ilmenite has ~48.9

167 wt% TiO_2 and ~49.1 wt% ΣFeO on average, corresponding to $Ilm_{93}Hem_7$ (Table 1).

168 The lamellae contain up to 88-92 wt% ΣFeO and 1-6 wt% TiO_2 (Table 1). The

8

169 magnetite lamellae have TiO_2 contents negatively correlated with their sizes, and the

170 ultrafine lamellae have the highest TiO_2 content (Table 1). However, ultrafine

171 lamellae may be affected by the host ilmenite and exhibit quite similar color in BSE

172 images to the coarse lamellae (Fig. 2e), thus different-sized magnetite lamellae may

173 have similar TiO_2 content. This is supported by our previous micro-XRD results

174 showing that the exsolved magnetite has a cell parameter of $a_0 \approx 8.394$ Å (Tan et al.

175 2015b), identical to that of pure magnetite (Wechsler et al. 1984). The cell

176 parameter of $Fe_{3-x}Ti_xO_4$ (x = 0~1) is supposed to have a positive correlation with

177 TiO_2 content and can be calculated using $a_0 = 8.3957 + 0.0688x + 0.1957x^2 -$

178 $0.1247x^3$ (x = 0~1, r^2 = 0.9995) (Wechsler et al. 1984). If the ultrafine magnetite

179 lamellae have ~5.30 wt% TiO_2 in the lattice (Table 1), the cell parameter would

180 approach to 8.410 Å, higher than the value we obtained by XRD results (Tan et al.

181 2015b). We thus consider that at least ~1 wt% TiO_2 is actually from the ultrafine

182 magnetite lamellae in host ilmenite.

183 **Crystallographic relationships**

184 EBSD Kikuchi patterns reflect the 3D orientation of the lattice planes/directions

185 of the test points in reference to the sample plane. Kikuchi patterns were collected

186 from a number of magnetite lamellae and host ilmenite in this study. The Kikuchi

187 patterns for the host ilmenite and >1 μm-wide magnetite lamellae were well indexed

188 as $R\bar{3}$ ilmenite (Fig. 4b) and Fd3m magnetite (Figs. 4c and 4d), respectively. The

189 indexed Kikuchi patterns provide additional evidence for the phase identification of

190   the magnetite lamellae, and also indicate that the magnetite lamellae have two

191   different crystallographic orientations in the host ilmenite (Figs. 4c and 4d).

192   The crystallographic relationship of magnetite lamellae and host ilmenite can be

193   determined if we can find a plane and an in-plane direction parallelism between the

194   lattices of the two phases (Li et al. 2011). Eight ilmenite grains with magnetite

195   lamellae of different size exhibit identical crystallographic relationships (Fig. S2). One

196   representative EBSD result is presented in form of upper-hemisphere stereographic

197   projection of mineral crystallographic orientation (Fig. 5). The host ilmenite has the

198   same orientation with negligible variation (Fig. 5a), indicating that the host ilmenite

199   is single crystal. The magnetite lamellae have two crystallographic orientations

200   sharing a $\{111\}_{Mag}$ plane and a corresponding set of $<110>_{Mag}$ directions within

201    $\{111\}_{Mag}$ plane (Fig. 5b), which are shown as $\{111\}_{Mag}$ planes and $<110>_{Mag}$

202   directions when the magnetite crystal rotates around L^3 symmetry axis $<111>$ for

203   60° in the modeling (Fig. 6). Note that the shared $\{111\}_{Mag}$ plane and corresponding

204   set of $<110>_{Mag}$ directions are parallel to $(0001)_{Ilm}$ and $<10\text{-}10>_{Ilm}$, respectively (Fig.

205   5a). Given the symmetry of ilmenite and magnetite, the EBSD results indicate that

206   the magnetite lamellae and the host ilmenite have a crystallographic relationship of

207    $\{111\}_{Mag} // (0001)_{Ilm}$ and $<110>_{Mag} // <10\text{-}10>_{Ilm}$.

208

209   **DISCUSSION**

210   **Formation of magnetite lamellae in ilmenite**

211   Ilmenite has a hexagonal crystal structure with the space group R$\bar{3}$, and

212   magnetite has a cubic crystal structure with the space group Fd3m (Waychunas

213   1991). They both consist of close-packed arrangement of oxygen atoms and stacked

214   cation layers in crystal lattice. The close packing of oxygen atoms plays an important

215   role in determining orientations of the exsolved magnetite (Barbosa et al. 2010;

216   Wenk et al. 2011). Thus, the close-packed oxygen atom planes and directions in host

217   ilmenite and exsolved magnetite are mainly investigated in this study. The

218   arrangement of oxygen atoms in magnetite is "cubic closest packing". The oxygen

219   atoms are close-packed in the $\{111\}_{Mag}$ planes and along the $<110>_{Mag}$ directions.

220   Oxygen atoms in ilmenite form a "hexagonal closest packing", and the close-packed

221   oxygen atom plane and directions are $(0001)_{Ilm}$ and $<10\text{-}10>_{Ilm}$, respectively. The

222   crystallographic relationships of $\{111\}_{Mag}$ // $(0001)_{Ilm}$ and $<110>_{Mag}$ // $<10\text{-}10>_{Ilm}$

223   (Fig. 6) indicate that the close-packed oxygen planes and directions in the two

224   phases are parallel.

225   The specific crystallographic relationships indicate that the magnetite lamellae

226   exsolved from ilmenite. Along the specific crystallographic orientation, The misfit (δ)

227   in vector lengths between $[110]_{Mag}$ and $[10\text{-}10]_{Ilm}$ is ~2.3% and there is no angle

228   misfit between them (Fig. S3). The oxygen framework of magnetite fits well with that

229   of ilmenite to minimize the strain energy at their interface (Fleet 1982; Xu et al. 2015;

230   Zhang et al. 2011). The close-packed oxygen framework forms a coherent interface

231   between the two phases (Trivedi 1970). The orientation of the magnetite lamellae is

232   thus considered to be controlled primarily by the coherent oxygen interface in

233   growth. However, the oxygen framework has to be transformed from a "hexagonal

234   closest packing" into a "cubic closest packing" with the crystallization of magnetite.

235   This transformation can be achieved by a "faulting mechanism" that is analogue to

236   the "fcc-hcp" martensitic transformation in Fe-Cr-Ni alloys (Olson and Cohen 1976)

237   and the quasi-martensitic transformation of olivine to spinel (Price et al. 1979; Price

238   et al. 1982).

Origin of Fe^{2+} in exsolved magnetite

240   The solubility of $FeTiO_3$ in Fe_3O_4 or vice versa, has been experimentally proved to

241   be negligible (Lindsley 1962, 1963; Lattard et al. 2006). Although small amounts of

242   ilmenite ($FeTiO_3$) can exsolve directly from cation-deficient titanomagnetite solid

243   solution by substitution of Ti^{4+} + □ ⮀ $2Fe^{2+}$ (Lattard 1995), cation-deficient ilmenite

244   solid solution formed in a similar way should exsolve TiO_2 rather than Fe_3O_4 during

245   cooling. Therefore, it seems implausible that magnetite lamellae in ilmenite could

246   directly exsolve from a Fe_3O_4-$FeTiO_3$ precursor.

247   Ilm-Hem$_{ss}$ contains variable amounts of Fe^{3+} in a wide range of oxygen fugacity

248   and temperature (Buddington and Lindsley 1964; Evans and Scaillet 1997; Sauerzapf

249   et al. 2008), however, decomposition of Ilm-Hem$_{ss}$ can only produce hematite

250   ($Fe^{3+}_2O_3$) lamellae in ilmenite. On the other hand, decomposition of $Fe^{2+}TiO_3$ portion

251   in Ilm-Hem$_{ss}$ generates not only Fe^{2+}, but also Ti^{4+}, whereas Ti-rich phases such as

252   rutile, have not been observed in host ilmenite (Fig. 2). As magnetite ($Fe^{2+}Fe^{3+}_2O_4$)

12

253 contains both Fe^{2+} and Fe^{3+}, the origin of Fe^{2+} in the exsolved magnetite in ilmenite

254 seems enigmatic.

255   The exsolution process probably not only involves transformation of oxygen

256 framework but also re-equilibration of intra-oxide and even inter-oxide cations. The

257 origin of Fe^{2+} in the exsolved magnetite could be ascribed to the subsolidus reduction

258 of Fe^{3+} in Ilm-Hem$_{ss}$ precursor, as shown by Equation (1) (Buddington and Lindsley

259 1964; Evans et al. 2006),

260          $$6Fe_2O_{3 \text{ in Ilm-Hem ss}} = 4Fe_3O_{4 \text{ exsolution}} + O_2 \dots \text{Equation (1)}.$$

261 However, the exsolved magnetite formed by subsolidus reduction tends to have

262 relatively high Ti^{4+} or Fe_2TiO_4 content (Haggerty 1991), which is inconsistent with

263 the low TiO_2 content of the magnetite lamellae in ilmenite in this study (Table 1).

264 Note that the titanomagnetite adjacent to the ilmenite has two distinctive

265 generations of ilmenite lamellae, Ilm-I and Ilm-II (Fig. 2f). The trellis-like Ilm-II is

266 formed by the oxidation of titanomagnetite under relatively oxidized condition (Tan

267 et al. 2015b), it is thus implausible that the reversed host-guest intergrowth is

268 ascribed to fO_2 fluctuation in the interstitial fluid, as suggested by the model of

269 Buddington and Lindsley (1964). The Fe^{2+} in the magnetite lamellae is thus unlikely

270 caused by intra-oxide cation re-equilibration (decomposition or reduction) in the

271 Ilm-Hem$_{ss}$ precursor.

272   Ilm-Hem$_{ss}$ and titanomagnetite tend to experience extensive sub-solidus

273 re-equilibration on cooling, represented by the cation exchange reaction between

13

274   the oxides (2) (Frost 1991),

275   Fe_2TiO_4 in titanomagnetite $+ Fe_2O_3$ in Ilm-Hemss $= FeTiO_3$ ilmenite $+ Fe_3O_4$ magnetite

276   ... Equation (2).

277   This reaction proceeds to the right with decreasing temperature, and Ilm-Hem$_{ss}$ and

278   titanomagnetite approach the end-members of Fe_3O_4 and $FeTiO_3$, respectively. An

279   experimental result indicate that the inter-oxide re-equilibration could function in

280   an O_2-conserving condition (Lattard 1995). In the experiment, samples were

281   prepared in two steps: (1) polycrystalline titanomagnetite $+$ Ilm-Hem$_{ss}$ assemblage

282   was synthesized from oxide mixtures in a Fe-Ti-Cr-O system at 1300 °C under oxygen

283   fugacity (fO_2) from 10^{-11} to $10^{-8.5}$, both titanomagnetite and Ilm-Hem$_{ss}$ have

284   homogeneous compositions; (2) fragments of starting samples were annealed at

285   temperature from 1100 to 700 °C in vacuo for different duration (Lattard 1995). The

286   annealing results indicate that the samples synthesized at the highest fO_2 ($10^{-8.5}$ at

287   1300 °C) exhibited reversed host-guest intergrowth of magnetite and ilmenite

288   (Lattard 1995), similar to that in this study. This intergrowth was attributed to a

289   combined function of vacancy relaxation and $Fe^{2+}Ti^{4+}Fe^{3+}_{-2}$ exchange between

290   titanomagnetite and Ilm-Hem$_{ss}$ (Lattard 1995). Therefore, we consider that the Fe^{2+}

291   in the exsolved magnetite in this study is probably derived from adjacent

292   titanomagnetite by intra-oxide cation re-equilibration, whereas the bulk

293   compositions of coexisting titanomagnetite and ilmenite remain constant.

294   The diffusion rates of Fe and Ti in Ilm-Hem$_{ss}$ are considered to be competitive,

14

295   as Fe^{2+}, Fe^{3+} and Ti^{4+} have equivalent cation occupancy in the Ilm-Hem$_{ss}$ structure

296   (McEnroe et al. 2002). However, it is shown that Fe^{2+} diffuses one to two orders of

297   magnitude faster than Ti^{4+} in titanomagnetite (Aragon et al. 1984), leading to

298   occupancy of Fe^{2+} in Ilm-Hem$_{ss}$ and crystallization of magnetite lamellae. On the

299   other hand, residual Ti^{4+} and related $Fe^{2+}_2TiO_4$ in adjacent titanomagnetite could

300   "precipitate" as ilmenite at the titanomagnetite-ilmenite interface or form ilmenite

301   lamellae in the titanomagnetite, resulting in the formation of a lamella-free zone in

302   the margin of the ilmenite (Fig. 2d) and lentiform ilmenite exsolution (Ilm-I) within

303   the titanomagnetite (Fig. 2f).

304   **Formation condition for different exsolution types in ilmenite**

305   Fe-Ti oxides in plutonic rocks experience extensive sub-solidus re-equilibration

306   during   slow   cooling,   including   oxide-silicate   re-equilibration,   inter-oxide

307   re-equilibration and intra-oxide re-equilibration (Frost 1991). Ilm-Hem$_{ss}$ tends to

308   exhibit different types of exsolution with different T-fO_2 cooling trends. The T-fO_2

309   cooling trends are primarily controlled by the factors such as original oxygen fugacity

310   of   the   host   rock,   relative   abundance   of   titanomagnetite   and   ilmenite,   and

311   composition of fluids (e.g. H_2O and CO_2) (Frost 1991). If Ilm-Hem$_{ss}$ is dominant phase

312   in the rock, the cooling trend would follow the T-fO_2 isopleths of Ilm-Hem$_{ss}$, and the

313   hematite   exsolution   would   occur   in   ilmenite   by   intra-oxide   re-equilibration   of

314   Ilm-Hem$_{ss}$ when temperature falls below the solvus.

315   In contrast, titanomagnetite makes up 40-50% and ilmenite makes up 20-30% of

15

316 the samples in this study, the titanomagnetite is thus the dominant phase in the

317 samples. A previous study indicated that the cooling trend of the upper part of the

318 Xinjie intrusion follows the T-fO_2 isopleths of titanomagnetite (Wang et al. 2008). The

319 Ilm-Hem$_{ss}$ and coexisting titanomagnetite would have extensive sub-solidus

320 inter-oxide re-equilibration following this cooling trend as discussed above. If this is

321 the case, magnetite rather than hematite exsolution occurs in ilmenite. On the other

322 hand, the titanomagnetite tends to be oxidized by fluids at relatively low temperature

323 with occurrence of intracrystalline ilmenite exsolution (Buddington and Lindsley

324 1964; Frost 1991), thus forming trellis-like ilmenite lamellae (Ilm-II) in

325 titanomagnetite.

326

327 **IMPLICATIONS**

328   This study indicates that both magnetite ($Fe^{2+}Fe^{3+}_2O_4$) and hematite ($Fe^{3+}_2O_3$)

329 exsolved from host ilmenite when the Ilm-Hem$_{ss}$ precursor experienced different

330 sub-solidus re-equilibration. Detailed characterization for the micro-intergrowth in

331 host ilmenite and intracrystalline exsolved phases is crucial for reconstructing the

332 composition of Ilm-Hem$_{ss}$ precursor and for application to the Fe-Ti oxide

333 oxy-thermometer. In the case of hematite exsolution from ilmenite, the composition

334 of the Ilm-Hem$_{ss}$ precursor can be reconstructed by simply integrating and averaging

335 the chemistry of exsolved hematite with that of the host ilmenite. In the case of

336 magnetite exsolution from ilmenite, the Fe^{2+} in magnetite is released from adjacent

16

337   titanomagnetite, whereas the Fe^{3+} in the magnetite lamellae should be included into

338   the Ilm-Hem$_{ss}$ precursor.

339   Magnetite exsolution is suggested to occur at temperatures above the

340   ilmenite-hematite miscibility gap at 600–700 °C (Lindsley 1991, Harrison et al. 2000).

341   Below 600 °C, Fe^{3+} in Ilm-Hem$_{ss}$ tends to exsolve directly as hematite rather than

342   magnetite. As magnetite exsolution in ilmenite occurs above its Curie temperature at

343   580 °C (Dunlop and Özdemir 2007), the exsolved magnetite can serve as an

344   important potential NRM source in plutonic rocks. The unusual magnetic properties

345   of natural ilmenite has been attributed to a ferrimagnetic substructure created by

346   ferrous–ferric "contact layers" at the hematite-ilmenite interface (Harrison 2006;

347   Kasama et al. 2003, 2009; McEnroe et al. 2001, 2002; Robinson et al. 2002, 2004).

348   Because the saturated magnetization of ferromagnetic magnetite (92 Am^2kg^{-1}) is

349   almost 230 times higher than antiferromagnetic hematite (0.4 Am^2kg^{-1}) (O'reilly

350   1984), the occurrence of magnetite exsolution in ilmenite may provide an alternative

351   explanation for the strong NRM in some natural ilmenite.

352

17

358 **REFERENCES CITED**

359 Andersen, D.J., and Lindsley, D.H. (1988) Internally consistent solution models for

360   Fe-Mg-Mn-ti oxides: Fe-Ti oxides. The American Mineralogist, 73, 714-726.

361 Aragon, R., McCallister, R., and Harrison, H. (1984) Cation diffusion in

362   titanomagnetites. Contributions to Mineralogy and Petrology, 85, 174-185.

363 Barbosa, P.F., and Lagoeiro, L. (2010) Crystallographic texture of the

364   magnetite-hematite transformation: Evidence for topotactic relationships in

365   natural samples from Quadrilátero Ferrífero, Brazil. American Mineralogist, 95,

366   118-125.

367 Bolle, O., Charlier, B., Bascou, J., Diot, H., and McEnroe, S.A. (2014) Anisotropy of

368   magnetic susceptibility versus lattice-and shape-preferred orientation in the

369   Lac Tio hemo-ilmenite ore body (Grenville province, Quebec). Tectonophysics,

370   629, 87-108.

371 Brownlee, S.J., Feinberg, J.M., Harrison, R.J., Kasama, T., Scott, G.R., and Renne, P.R.

372   (2010) Thermal modification of hematite-ilmenite intergrowths in the Ecstall

373   pluton, British Columbia, Canada. American Mineralogist, 95, 153-160.

374 Buddington, A.F., and Lindsley, D.H. (1964) Iron-Titanium Oxide Minerals and

375   Synthetic Equivalents. Journal of petrology, 5, 310-357.

376 Dobrzhinetskaya, L., Green, H.W., II, and Wang, S. (1996) Alpe Arami: a peridotite

377   massif from depths of more than 300 kilometers. Science, 271, 1841.

378 Dong, H., Xing, C., and Wang, C.Y. (2013) Textures and mineral compositions of the

379   Xinjie layered intrusion, SW China: Implications for the origin of magnetite

380   and fractionation process of Fe-Ti-rich basaltic magmas. Geoscience Frontiers,

381   4, 503-515.

382   Dunlop, D., and Özdemir, Ö. (2007) Magnetizations in rocks and minerals. Treatise

383   on Geophysics, 5, 277-336.

384   Evans, B.W., and Scaillet, B. (1997) The redox state of Pinatubo dacite and the

385   ilmenite-hematite solvus. American Mineralogist, 82, 625-629.

386   Evans, B.W., Scaillet, B., and Kuehner, S.M. (2006) Experimental determination of

387   coexisting iron–titanium oxides in the systems FeTiAlO, FeTiAlMgO,

388   FeTiAlMnO, and FeTiAlMgMnO at 800 and 900 C, 1–4 kbar, and relatively high

389   oxygen fugacity. Contributions to Mineralogy and Petrology, 152, 149-167.

390   Feinberg, J.M., Wenk, H.R., Renne, P.R., and Scott, G.R. (2004) Epitaxial

391   relationships of clinopyroxene-hosted magnetite determined using electron

392   backscatter diffraction (EBSD) technique. American Mineralogist, 89,

393   462-466.

394   Feinberg, J.M., Scott, G.R., Renne, P.R., and Wenk, H.R. (2005) Exsolved magnetite

395   inclusions in silicates: Features determining their remanence behavior.

396   Geology, 33(6), 513-516.

397   Ferré, E.C., Friedman, S.A., Martín-Hernández, F., Feinberg, J.M., Conder, J.A., and

398   Ionov, D.A. (2013) The magnetism of mantle xenoliths and potential

399   implications for sub-Moho magnetic sources. Geophysical Research Letters,

400   40, 105-110.

401   Fleet, M.E., Bilcox, G.A., and Barnett, R.L. (1980) Oriented magnetite inclusions in

402   pyroxenes from the Grenville Province. Canadian Mineralogist, 18, 89-99.

403   Fleet, M.E. (1982) Orientation of phase and domain boundaries in crystalline solids.

404   American Mineralogist, 67, 926-936.

405   Frost, B.R. (1991) Magnetic petrology: factors that control the occurrence of

19

406   magnetite in crustal rocks. Reviews in Mineralogy and Geochemistry, 25,

407   489-509.

408 Haggerty, S.E. (1991) Oxide textures — a mini-atlas. Reviews in Mineralogy and

409   Geochemistry, 25, 129-219.

410 Harrison, R.J. Becker, U., Redfern, S.A.T. (2000) Thermodynamics of the $R\bar{3}$ to $R\bar{3}c$

411   phase transition in the ilmenite-hematite solid solution. American

412   Mineralogist, 85, 1694-1705.

413 Harrison, R.J. (2006) Microstructure and magnetism in the ilmenite-hematite

414   solid solution: A Monte Carlo simulation study. American Mineralogist, 91,

415   1006-1023.

416 Hwang, S.L., Yui, T.F., Chu, H.T., Shen, P., Iizuka, Y., Yang, H.Y., Yang, J., and Xu, Z.

417   (2008) Hematite and magnetite precipitates in olivine from the Sulu

418   peridotite: A result of dehydrogenation-oxidation reaction of mantle olivine?

419   American Mineralogist, 93, 1051-1060.

420 Joesten, R.L. (1991) Kinetics of coarsening and diffusion-controlled mineral

421   growth. Reviews in Mineralogy and Geochemistry, 26, 507-582.

422 Kasama, T., Golla-Schindler, U., and Putnis, A. (2003) High-resolution and

423   energy-filtered TEM of the interface between hematite and ilmenite

424   exsolution lamellae: Relevance to the origin of lamellar magnetism. American

425   Mineralogist, 88, 1190-1196.

426 Kasama, T., Dunin-Borkowski, R.E., Asaka, T., Harrison, R.J., Chong, R.K., McEnroe,

427   S.A., Simpson, E.T., Matsui, Y., and Putnis, A. (2009) The application of Lorentz

428   transmission electron microscopy to the study of lamellar magnetism in

429   hematite-ilmenite. American Mineralogist, 94, 262-269.

430   Lattard, D. (1995) Experimental-Evidence for the Exsolution of Ilmenite from
431   Titaniferous Spinel. American Mineralogist, 80, 968-981.

432   Lattard, D. Sauerzapf, U. and Kasemann, M. (2005) New calibration data for the
433   Fe-Ti oxide thermo-oxybarometers from experiments in the Fe-Ti-O system at
434   1 bar, 1,000-1,300 degrees C and a large range of oxygen fugacities.
435   Contributions to Mineralogy and Petrology, 149, 735-754.

436   Lattard, D., Engelmann, R., Kontny, A., and Sauerzapf, U. (2006) Curie temperatures
437   of synthetic titanomagnetites in the Fe-Ti-O system: Effects of composition,
438   crystal chemistry, and thermomagnetic methods. Journal of Geophysical
439   Research: Solid Earth, 111, B12S28.

440   Li, Z., Zhang, Y., Esling, C., Zhao, X., and Zuo, L. (2011) Determination of the
441   orientation relationship between austenite and incommensurate 7M
442   modulated martensite in Ni–Mn–Ga alloys. Acta Materialia, 59, 2762-2772.

443   Lindsley, D.H. (1962) Investigations in the system $FeO-Fe_2O_3-TiO_2$. Carnegie
444   Institution of Washington Yearbook, 61, 100-106.

445   ——— (1963) Equilibrium relations of coexisting pairs of Fe-Ti oxides. Carnegie
446   Institution of Washington Year Book, 62, 60-66.

447   ——— (1991) Experimental studies of oxide minerals. Reviews in Mineralogy and
448   Geochemistry, 25, 69-106.

449   Mücke, A. (2003) Magnetite, ilmenite and ulvite in rocks and ore deposits:
450   petrography, microprobe analyses and genetic implications. Mineralogy and
451   Petrology, 77, 215-234.

452   McEnroe, S.A., Robinson, P., and Panish, P.T. (2001) Aeromagnetic anomalies,
453   magnetic petrology, and rock magnetism of hemo-ilmenite-and
454   magnetite-rich cumulate rocks from the Sokndal Region, South Rogaland,

21

455   Norway. American Mineralogist, 86, 1447-1468.

456   McEnroe, S.A., Harrison, R., Robinson, P., and Langenhorst, F. (2002) Nanoscale

457   haematite–ilmenite lamellae in massive ilmenite rock: an example of 'lamellar

458   magnetism' with implications for planetary magnetic anomalies. Geophysical

459   Journal International, 151, 890-912.

460   Morisset, C.E., Scoates, J.S., Weis, D., Sauvé, M., and Stanaway, K.J. (2010)

461   Rutile-bearing ilmenite deposits associated with the Proterozoic Saint-Urbain

462   and Lac Allard anorthosite massifs, Grenville Province, Quebec. The Canadian

463   Mineralogist, 48, 821-849.

464   Morisset, C.E., Williamson, M.C., Hipkin, V., and Sylvester, P. (2013) Investigation

465   of three Fe–Ti oxide deposits associated with Grenvillian anorthosite massifs

466   as potential source for lunar analogue ilmenite. Canadian Journal of Earth

467   Sciences, 50, 64-77.

468   O'reilly, W. (1984) Rock and mineral magnetism. Springer Science & Business

469   Media. p.172-191, Blackie, Glasgow.

470   Olson, G., and Cohen, M. (1976) A general mechanism of martensitic nucleation:

471   Part I. General concepts and the FCC⊡HCP transformation. Metallurgical

472   Transactions A, 7, 1897-1904.

473   Price, G.D., Putnis, A., and Agrell, S. (1979) Electron petrography of

474   shock-produced veins in the Tenham chondrite. Contributions to Mineralogy

475   and Petrology, 71, 211-218.

476   Price, G.D. (1980) Exsolution microstructures in titanomagnetites and their

477   magnetic significance. Physics of the Earth and Planetary Interiors, 23, 2-12.

478   Price, G.D., Putnis, A., and Smith, D. (1982) A spinel to β-phase transformation

479   mechanism in $(Mg, Fe)_2SiO_4$. Nature, 296, 729-731.

480   Prior, D.J., Boyle, A.P., Brenker, F., Cheadle, M.C., Day, A., Lopez, G., Peruzzo, L., Potts,

481   G.J., Reddy, S., and Spiess, R. (1999) The application of electron backscatter

482   diffraction and orientation contrast imaging in the SEM to textural problems

483   in rocks. American Mineralogist, 84, 1741-1759.

484   Robinson, P., Harrison, R.J., McEnroe, S.A., and Hargraves, R.B. (2002) Lamellar

485   magnetism in the haematite–ilmenite series as an explanation for strong

486   remanent magnetization. Nature, 418, 517-520.

487   ——— (2004) Nature and origin of lamellar magnetism in the hematite-ilmenite

488   series. American Mineralogist, 89, 725-747.

489   Shebanova, O.N., and Lazor, P. (2003a) Raman study of magnetite (Fe_3O_4):

490   laser-induced thermal effects and oxidation. Journal of Raman spectroscopy,

491   34, 845-852.

492   ——— (2003b) Raman spectroscopic study of magnetite ($FeFe_2O_4$): a new

493   assignment for the vibrational spectrum. Journal of Solid State Chemistry,

494   174, 424-430.

495   Sauerzapf, U., Lattard, D., Burchard, M., and Engelmann, R. (2008) The

496   titanomagnetite–ilmenite equilibrium: new experimental data and

497   thermo-oxybarometric application to the crystallization of basic to

498   intermediate rocks. Journal of petrology, 49, 1161-1185.

499   Tan, W., Wang, C.Y., He, H.P., Xing, C., Liang, X.L., and Dong, H. (2015a)

500   Magnetite-rutile symplectite derived from ilmenite-hematite solid solution in

501   the Xinjie Fe-Ti oxide-bearing, mafic-ultramafic layered intrusion (SW China).

502   American Mineralogist, 100, 2348-2351.

503   Tan, W., Wang, C.Y., He, H.P., Liang, X.L., and Liu, P. (2015b) Mineralogy and origin

504   of exsolution in the titanomagnetite of different magamatic Fe-Ti

505   oxide-bearing intrusions. The Canadian Mineralogist, in press.

506 Trivedi R. (1970) The role of interfacial free energy and interface kinetics during

507   the growth of precipitate plates and needles. Metallurgical Transactions, 1,

508   921-927.

509 Wang, A., Kuebler, K.E., Jolliff, B.L., and Haskin, L.A. (2004) Raman spectroscopy of

510   Fe-Ti-Cr-oxides, case study: Martian meteorite EETA79001. American

511   Mineralogist, 89, 665-680.

512 Wang, C.Y., Zhou, M.F., and Zhao, D.G. (2008) Fe-Ti-Cr oxides from the Permian

513   Xinjie mafic-ultramafic layered intrusion in the Emeishan large igneous

514   province, SW China: Crystallization from Fe- and Ti-rich basaltic magmas.

515   Lithos, 102, 198-217.

516 Waychunas, G.A. (1991) Crystal chemistry of oxides and oxyhydroxides. Reviews in

517   Mineralogy and Geochemistry, 25, 11-68.

518 Wechsler, B.A., Lindsley, D.H., and Prewitt, C.T. (1984) Crystal structure and cation

519   distribution in titanomagnetites ($Fe_{3-x}Ti_xO_4$). American Mineralogist, 69,

520   754-770.

521 Wenk, H.R., Chen, K., and Smith, R. (2011) Morphology and microstructure of

522   magnetite and ilmenite inclusions in plagioclase from Adirondack anorthositic

523   gneiss. American Mineralogist, 96, 1316-1324.

524 Xu, H., Zhang, J., Zong, K., and Liu, L. (2015) Quartz exsolution topotaxy in

525   clinopyroxene from the UHP eclogite of Weihai, China. Lithos, 226, 17-30.

526 Zhang, J., Xu, H., Liu, Q., Green, H., and Dobrzhinetskaya, L. (2011) Pyroxene

527   exsolution topotaxy in majoritic garnet from 250 to 300 km depth. Journal of

528   Metamorphic Geology, 29, 741-751.

529 Zhong, H., Yao, Y., Prevec, S.A., Wilson, A.H., Viljoen, M.J., Viljoen, R.P., Liu, B.G., and

530   Luo, Y.N. (2004) Trace-element and Sr–Nd isotopic geochemistry of the

531   PGE-bearing Xinjie layered intrusion in SW China. Chemical Geology, 203,

532   237-252.

533 Zhou, M.F., Yan, D.P., Kennedy, A.K., Li, Y., and Ding, J. (2002) SHRIMP U–Pb zircon

534   geochronological and geochemical evidence for Neoproterozoic

535   arc-magmatism along the western margin of the Yangtze Block, South China.

536   Earth and Planetary Science Letters, 196, 51-67.

537 Zhou, M.F., Robinson, P.T., Lesher, C.M., Keays, R.R., Zhang, C.J., and Malpas, J.

538   (2005) Geochemistry, petrogenesis and metallogenesis of the Panzhihua

539   gabbroic layered intrusion and associated Fe-Ti-V oxide deposits, Sichuan

540   Province, SW China. Journal of petrology, 46, 2253-2280.

541

542

FIGURE CAPTIONS

544

FIGURE 1. (a) Geological map showing the distribution of the Fe-Ti oxide-bearing

mafic-ultramafic layered intrusions in the Panxi region, SW China (modified after

Zhou et al. 2002; Zhong et al. 2004; Dong et al. 2013); **(b)** A stratigraphic column

of the rock units showing the distribution of major rock and ore types in the Xinjie

intrusion (modified after Dong et al. 2013) and sample location.

550

FIGURE 2. Photomicrograph (a) and BSE images (b-f) of the Fe-Ti oxide gabbro in

Unit III of the Xinjie intrusion. **(a)** Fe-Ti oxides are interstitial to plagioclase (Pl)

and clinopyroxene (Cpx). Under plane-polarizer and transmitted light; **(b)**

Coexisting euhedral-subhedral titanomagnetite (Tmt) and ilmenite (Ilm). Note the

ilmenite lamellae in titanomagnetite versus magnetite lamellae in ilmenite; **(c)**

Lentiform magnetite lamellae in ilmenite range in width from > 10 μm (aspect

ratio ~5:1) to ~5 μm (aspect ratio ~10:1); **(d)** Thin-plate magnetite lamellae in

the ilmenite are ~2 μm in width (aspect ratio ~15:1). Note that the host ilmenite

has a halo of lamella-free zone in the margin, as outlined by the red dash line; **(e)**

Ultrafine magnetite lamellae in the ilmenite are ~1 μm in width (aspect ratio

~50:1). Note that the coarse lamellae in the central part of the host ilmenite have

a halo of lamella-free zone in the margin, as outlined by the green dash line; **(f)**

The titanomagnetite adjacent to ilmenite develops two generations of ilmenite

lamellae, i.e. oriented lentiform ilmenite lamellae (Ilm-I) and   trellis-like ilmenite

26

565   lamellae (Ilm-II).

566

567   **FIGURE 3.** Raman spectra of lamellae in the ilmenite from the Xinjie intrusion. **(a)**

568   Raman spectra for the lamellae with different widths; **(b)** Peak deconvolution of

569   the Raman spectrum for the ultrafine lamellae (width = ~1 μm) in ilmenite using

570   program PeakFit v4.12. Note that the main band at 674 cm^{-1} was optimally fitted

571   with the Gaussian + Lorentzian bands at 669 (green dash line) and 683 cm^{-1}

572   (orange dash line), corresponding to the bands of magnetite and host ilmenite,

573   respectively, regression coefficient (r^2) of the peak-fit analysis approaches 0.999,

574   more details see Supplemental Material-Table S2.

575

576   **FIGURE 4. (a)** BSE images of magnetite lamellae in the ilmenite from the Xinjie

577   intrusion; **(b-d)** Original (right corner) and automatically indexed Kikuchi

578   patterns of the host ilmenite and magnetite lamellae b, c and d shown in **(a).** Note

579   that **(c)** and **(d)** represent two different crystallographic orientations of the
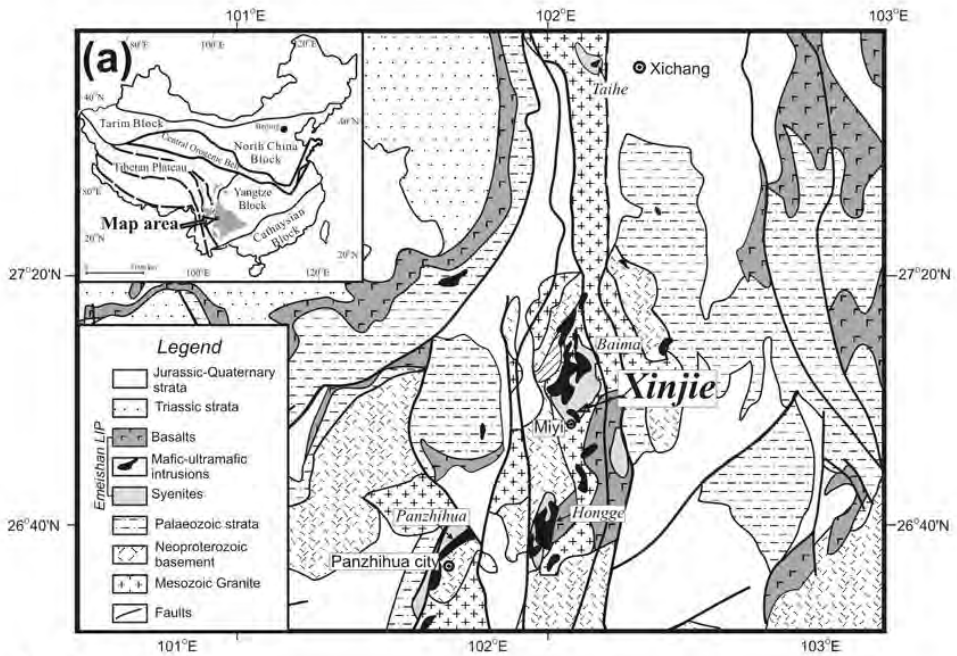
580   magnetite lamellae.

581

582   **FIGURE 5.** Crystallographic orientation of host ilmenite and magnetite lamellae

583   from one ilmentie grain. **(a)** Upper hemisphere stereographic projections of

584   orientations of host ilmenite (38 data collected from different part of the

585   ilmenite); **(b)** Upper hemisphere stereographic projections of orientations of the

586   magnetite lamellae in host ilmenite (72 data collected from ~50 magnetite

587   lamellae). Two different orientations of magnetite lamellae are indicated by

588   triangles ($\triangle$) and squares ($\square$), respectively. Note that the orientations of the

589   shared $\{111\}_{Mag}$ plane and $<110>_{Mag}$ directions are also plotted in **(a)**.

590

591   **FIGURE 6.** Space filling models for the crystal structure of ilmenite (a) and

592   magnetite (b and c). Models (a) + (b) and (a) + (c) showing that two possible

593   orientations of magnetite lamellae have crystallographic relationships of $\{111\}_{Mag}$

594   // $(0001)_{Ilm}$ and $<110>_{Mag}$ // $<10\text{-}10>_{Ilm}$ with the host ilmenite. Note that rotating

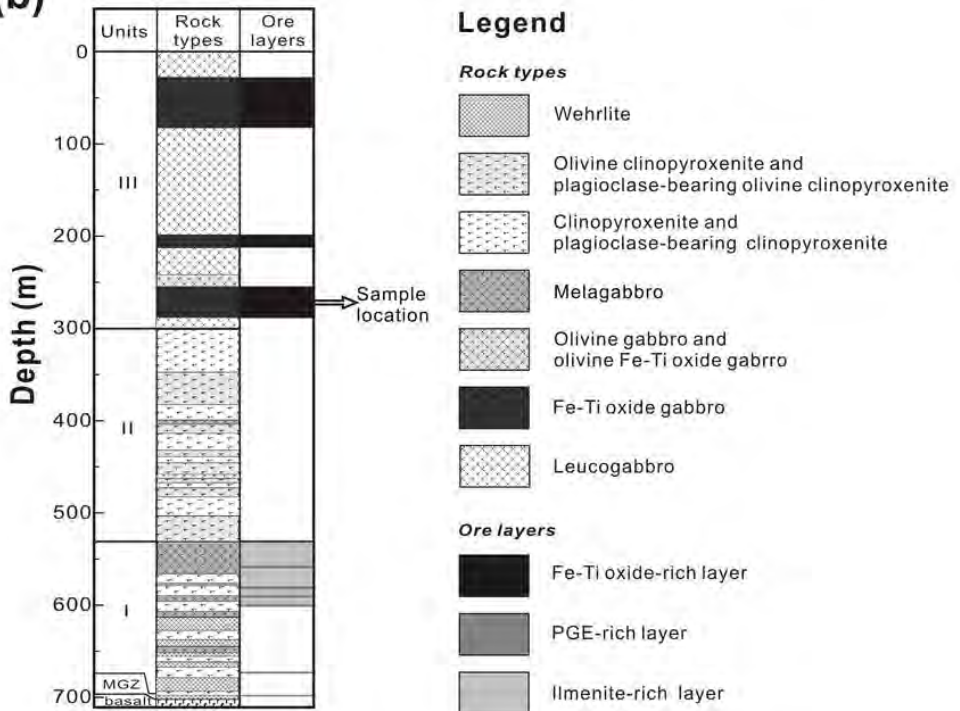595   model (b) around [111] for 60° makes model (c), and vice versa.

Figure 1

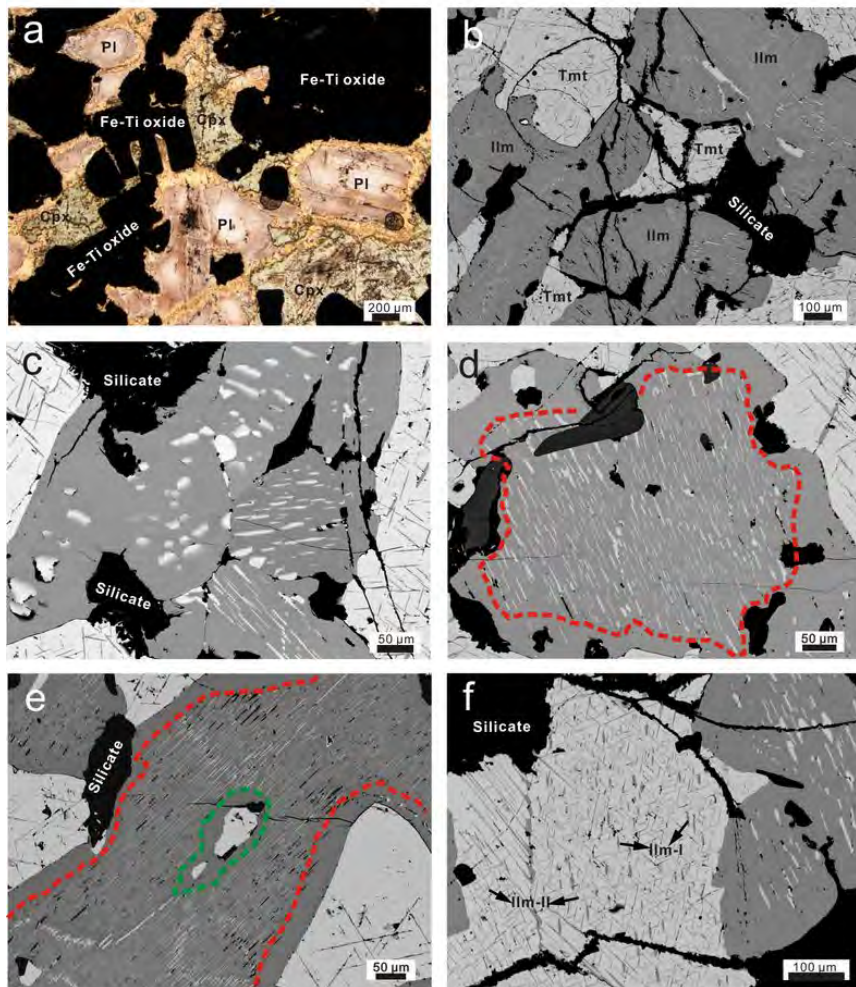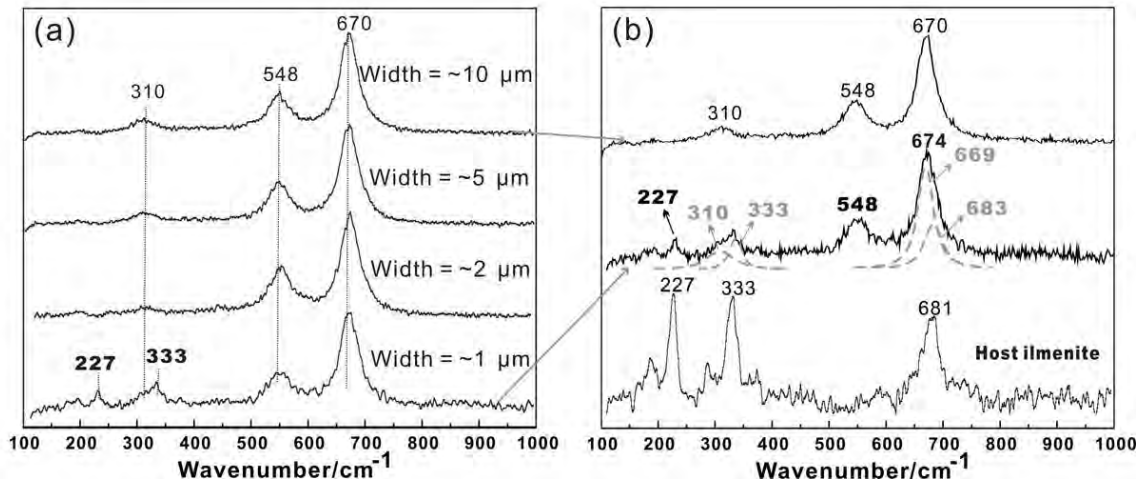# Figure 2

Figure 3

Figure 4

a — 20µm

b — $02\bar{2}\bar{1}$ $0\bar{3}\bar{3}\bar{1}$ $12\bar{3}\bar{1}$ $21\bar{3}\bar{1}$ $30\bar{3}\bar{1}$
EBSP of ilmenite

c — 031 021 011 012 013 $\bar{1}21$ $\bar{1}12$ $\bar{1}30$ $\bar{1}11$ $\bar{1}20$
EBSP of magnetite

d — 011 012 013 102 103 $\bar{1}12$ 001 $1\bar{1}2$ $\bar{1}03$ $\bar{1}02$ $0\bar{1}3$
EBSP of magnetite

Figure 5

(a) (0001) $\langle 11\bar{2}0 \rangle$ $\langle 10\bar{1}0 \rangle$ Host ilmenite 38 data

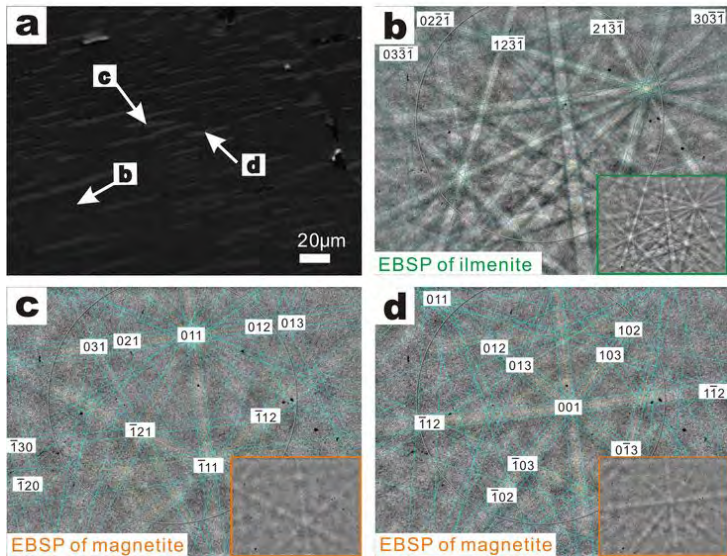(b) {111} $\langle 100 \rangle$ $\langle 110 \rangle$ Exsolved magnetite 72 data
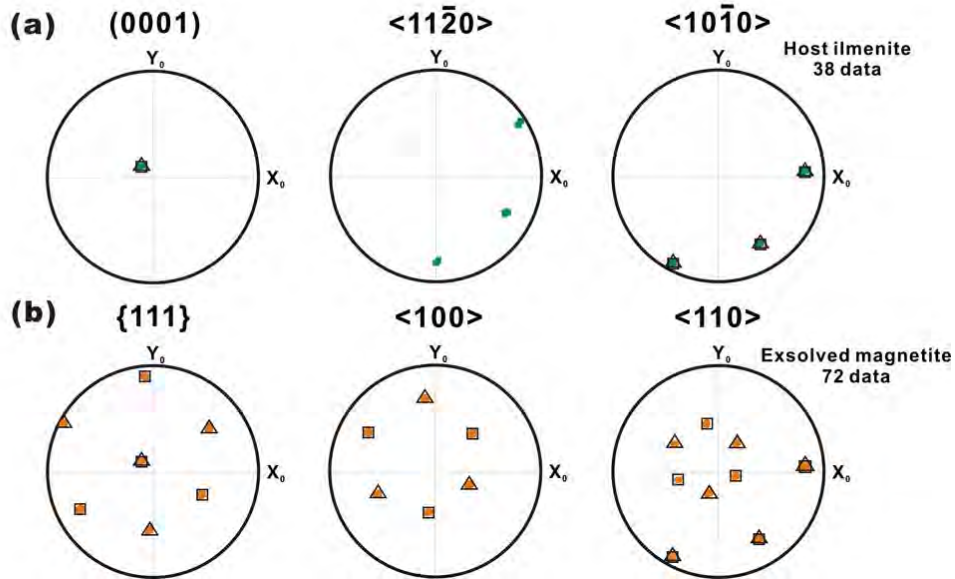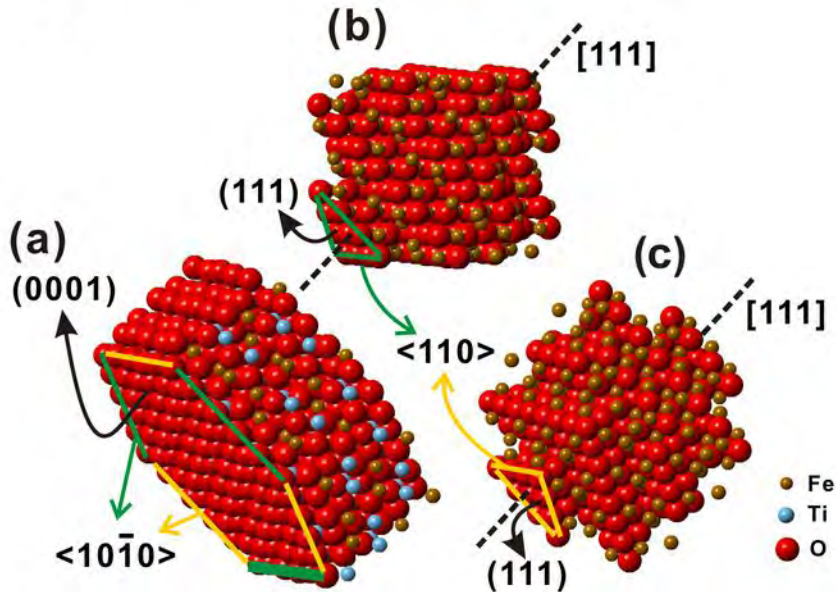
Figure 6

TABLE 1. Major oxide compositions (wt%) of ilmenite (Ilm) host and magnetite (Mgt) lamellae in the Xinjie intrusion

	Ilm host		Mgt lamellae (width > 10 μm)		Mgt lamellae (width = ~5 μm)		Mgt lamellae (width = ~2 μm)		Mgt lamellae (width = ~1 μm)	
	Avg (7)	STDV	Avg (5)	STDV	Avg (3)	STDV	Avg (4)	STDV	Avg (3)	STDV
SiO_2	0.01	0.01	-	-	0.01	0.01	-	-	0.01	0.01
MgO	0.49	0.05	0.01	0.01	-	-	0.02	0.01	0.04	0.02
Al_2O_3	0.00	0.01	0.10	0.03	0.02	0.01	0.07	0.03	0.09	0.07
ΣFeO	49.05	0.36	92.11	0.21	90.31	0.70	89.98	0.89	88.47	1.40
MnO	0.92	0.20	0.01	0.01	0.02	0.01	0.03	0.02	0.05	0.02
NiO	0.02	0.01	0.13	0.02	0.11	0.01	0.13	0.02	0.15	0.03
Cr_2O_3	0.01	0.01	0.08	0.02	0.08	0.02	0.08	0.02	0.06	0.01
V_2O_3	0.76	0.01	0.37	0.02	0.38	0.04	0.36	0.01	0.38	0.01
TiO_2	48.85	0.26	1.02	0.51	3.06	0.95	3.55	0.82	5.30	1.17
Total	100.11	0.26	92.92	0.50	93.99	0.49	94.22	0.20	94.54	0.21
Redistribution of ΣFeO										
FeO [a]	42.12		31.87		33.98		34.49		36.13	
Fe_2O_3 [a]	7.70		66.10		62.75		61.88		58.46	
Total [b]	100.88		99.68		100.41		100.62		100.66	

Notes: a- redistribution of ΣFeO between Fe_2O_3 and FeO is on the basis of charge balance and stoichiometry of magnetite and ilmenite respectively; b- total composition recalculated based on the values of FeO[a] and Fe_2O_3[a]. Avg (7) means that it is the averaged value for seven analytical results. STDV means standard deviation.